Solar Phys (2013) 284:47–58
DOI 10.1007/s11207-012-0209-0

Near-Sun Flux-Rope Structure of CMEs

H. Xie · N. Gopalswamy · O.C. St. Cyr

Received: 27 March 2012 / Accepted: 3 December 2012 / Published online: 4 January 2013

Abstract We have used the Krall flux-rope model (Krall and St. Cyr, *Astrophys. J.* 2006, **657**, 1740) (KFR) to fit 23 magnetic cloud (MC)-CMEs and 30 non-cloud ejecta (EJ)-CMEs in the Living With a Star (LWS) Coordinated Data Analysis Workshop (CDAW) 2011 list. The KFR-fit results shows that the CMEs associated with MCs (EJs) have been deflected closer to (away from) the solar disk center (DC), likely by both the intrinsic magnetic structures inside an active region (AR) and ambient magnetic structures (*e.g.* nearby ARs, coronal holes, and streamers, *etc.*). The mean absolute propagation latitudes and longitudes of the EJ-CMEs (18°, 11°) were larger than those of the MC-CMEs (11°, 6°) by 7° and 5°, respectively. Furthermore, the KFR-fit widths showed that the MC-CMEs are wider than the EJ-CMEs. The mean fitting face-on width and edge-on width of the MC-CMEs (EJ-CMEs) were 87 (85)° and 70 (63)°, respectively. The deflection away from DC and narrower angular widths of the EJ-CMEs have caused the observing spacecraft to pass over only their flanks and miss the central flux-rope structures. The results of this work support the idea that all CMEs have a flux-rope structure.

Keywords Coronal mass ejections · Initiation and propagation

Flux-Rope Structure of Coronal Mass Ejections
Guest Editors: N. Gopalswamy, T. Nieves-Chinchilla, M. Hidalgo, J. Zhang, and P. Riley

H. Xie (✉)
Solar Physics Lab, IACS/CUA – NASA Goddard Flight Center, Greenbelt, MD 20771, USA
e-mail: hong.xie@nasa.gov

N. Gopalswamy · O.C. St. Cyr
NASA Goddard Space Flight Center, Code 671, Greenbelt, MD 20771, USA

N. Gopalswamy
e-mail: nat.gopalswamy@nasa.gov

O.C. St. Cyr
e-mail: chris.stcyr@nasa.gov

1. Introduction

In recent years, a great deal of research in both modeling and observations (see, *e.g.*, Chen *et al.*, 1997; Dere *et al.*, 1999; Gibson and Low, 2000; Krall *et al.*, 2001; Cremades and Bothmer, 2004; Krall and St. Cyr, 2006; Thernisien, Howard, and Vourlidas, 2006; Krall, 2007) has been focused on coronal mass ejections (CMEs) having the "three-part" morphology, namely, a bright front, a dark void and a bright core of prominence material (Illing and Hundhausen, 1985). Concave-outward trailing features were noted in the *Solar Maximum Mission* (SMM) coronagraph images (Illing and Hundhausen, 1985; Burkepile and St. Cyr, 1993), but the high-resolution *Large Angle and Spectrometric COronagraph* (LASCO) observations revealed that these three-part CMEs often create the appearance of a helical or flux-rope (FR) structure.

The interplanetary (IP) counterpart of CMEs are called ICMEs. They are featured with high magnetic fields, low ion temperatures, high alpha/proton density ratios and occasionally bidirectional streaming of electrons and ions (*e.g.*, Gosling, 1990). Depending on whether they have a smooth rotating magnetic field, *i.e.*, a signature of flux rope, and fulfill other conditions, ICMEs are further classified into i) magnetic clouds (MCs), and ii) non-cloud ejecta (or simply ejecta) (EJs) (see, *e.g.*, Burlaga *et al.*, 1981; Gosling, 1990). Gopalswamy (2006) suggested that all CMEs have magnetic FR structures, but their propagation directions determine whether they can be seen *in-situ*.

Based on the coronagraphic observations, simple FR models of CMEs using a torus geometry have been developed by various authors. Krall and St. Cyr (2006) (hereafter KS06) described a FR model as having an elliptical curved axis with a circular cross-section of varying radius along the axis and the width (minor diameter) being narrowest at the footpoints on the solar surface. It was shown that the KS06 FR model (KFR) geometry reproduced the statistical measures (average angular widths) of a subset of FR-like CMEs observed by LASCO (St. Cyr *et al.*, 2004). Thernisien, Howard, and Vourlidas (2006) used the graduated cylindrical shell (GCS) model, a FR model with a conical curved axis, and demonstrated that the GCS model fits the CME morphologies for 34 FR-like CMEs selected from Cremades and Bothmer (2004). A more recent study (Krall, 2007) extended the work of KS06 by comparing the FR model synthetic images to 111 limb CMEs observed by SMM (Burkepile *et al.*, 2004). Their results suggested that the FR morphology can be applied not only to FR-like CMEs but also to the general population of CMEs.

In this work, we apply the KFR to the 2011 Living With a Star (LWS) Coordinated Data Analysis Workshop (CDAW) CME list to determine the radial speeds, angular widths, and the propagation directions of the CMEs. We studied 53 shock-driving CMEs during Solar Cycle 23 whose source regions are located within E15° and W15°. We have excluded complex event number 3 with multiple solar sources: an eruptive prominence (EP) (N45W10), active region (AR) 8115 (N32W32), and AR 8113 (N25W40). To zeroth order, it is supposed that MCs associated CMEs (MC-CMEs) come from the disk center, ejecta-CMEs come from intermediate longitudes, and driverless shocks come from near the limb (*e.g.*, Gopalswamy, 2006). Since all the CDAW CMEs originate nearly from the disk center, it is expected that they are observed as MCs at Earth, assuming that all CMEs have FR structures and erupt radially. However, for the 53 CDAW events, 23 events are associated with MCs and 30 events are EJs. One likely reason is the non-radial eruption of CMEs (see, *e.g.*, St. Cyr *et al.*, 2000; Gopalswamy *et al.*, 2009; Xie *et al.*, 2009). In this paper, we are looking into the characteristics that distinguish two CME populations: MC-CMEs and EJ-CMEs. By performing a detailed investigation of CME origins and propagations, we hope to answer the CDAW's focusing question: Do all CMEs have flux-rope structure, but sometimes they are not observed

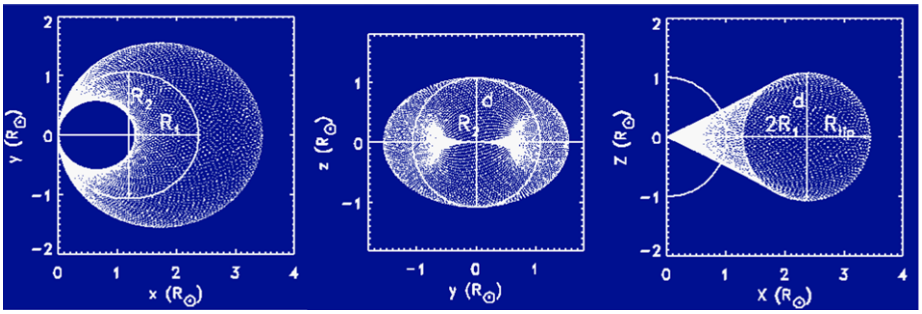

Figure 1 Illustrative plot of the flux-rope model morphology. From left to right: broadside (face-on), top, and edge-on views of a flux rope.

so because of geometry (the observing spacecraft does not pass through the flux rope) or do some CMEs have inherently non-flux-rope structure?

The rest of the paper is organized as follows. Section 2 describes data selection and detailed FR model fitting procedures. Section 3 presents the fitting results and statistical analysis. Finally, the summary and conclusions are presented in Section 4.

2. Data and Model

The CDAW 2011 list is a subset of the list in Gopalswamy *et al.* (2010). This subset was selected based on two criteria: i) the CMEs originate from close to the central meridian (E15° ≤ source longitude ≤ W15°), ii) the CMEs are associated with shock-driving interplanetary CMEs (ICMEs). The CDAW 2011 list consists of 23 MC-CMEs and 30 EJ-CMEs.

To determine the radial speeds, angular widths, and propagation directions of the CMEs, we applied the KS06 FR model fit (KFR-fit) to LASCO C2 and C3 images. The KS06 model is also called the elliptical FR model, which assumes that the FR has an elliptical axis with varying radial circular cross-sections. Figure 1 gives the broadside (face-on), top, and edge-on views of the FR model, with apex pointing to the west limb.

The geometry of the flux rope can be described by two parameters: the ratio of the semi-minor to semi-major axes of the ellipse, $\lambda_\epsilon = R_2/R_1$ and the axial aspect ratio, $\Lambda_\alpha = 2R_1/d$, where R_1, R_2, and d are semi-major axis, semi-minor axis and width of the flux rope at its apex, as shown in Figure 1. The orientation of the flux rope is defined by three angles: latitude λ, longitude ϕ, and tilt angle α, where the tilt angle is the rotation angle clockwise with respect to the East direction.

We used an iterative method to parameterize the flux-rope model. First, we chose initial test parameters of the model based on the coronagraphic observations; we then iteratively adjusted the test parameters until the best fit of the FR model to LASCO images was obtained. The fitted CME radial speed is given by $V_{\rm CME} = \Delta(R_{\rm tip})/{\rm d}t$, where $R_{\rm tip}$ is the radial distance from the origin to the apex of the FR. The widths of the CME are given by $\omega_{\rm edge} = 2 \times {\rm tg}^{-1}(0.5/\Lambda_\alpha)$, $\omega_{\rm broad} = 2 \times {\rm tg}^{-1}(\lambda_\epsilon)$, where $\omega_{\rm edge}$ and $\omega_{\rm broad}$ are the widths of the CME from edge-on and face-on views, respectively.

Figure 2 shows an example of the model fit for the 20 January 2004 CME. The CME was a halo CME associated with a C5.5 soft X-ray flare recorded by GOES in AR 10540 (S13W09), with a peak at 00:45 UT. The left panel of Figure 2 is an *Extreme Ultraviolet Imaging Telescope* (EIT) 195 Å image, which shows the post-eruption arcade titled ∼52°

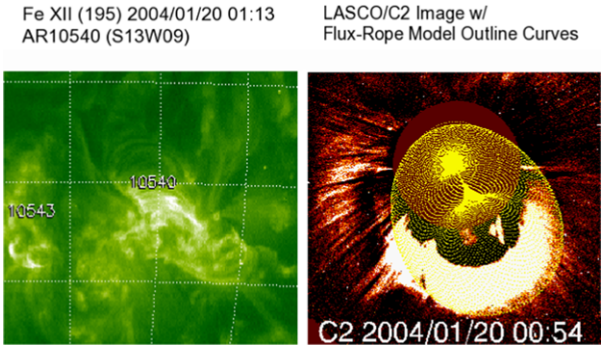

Figure 2 An example of the flux-rope model fit for the 20 January 2004 CME. (Left) EIT 195 Å image showing the flare post-eruption arcade at 01:13 UT. (Right) LASCO/C2 image at 00:54 UT superimposed with the flux-rope model outline curves (yellow curves).

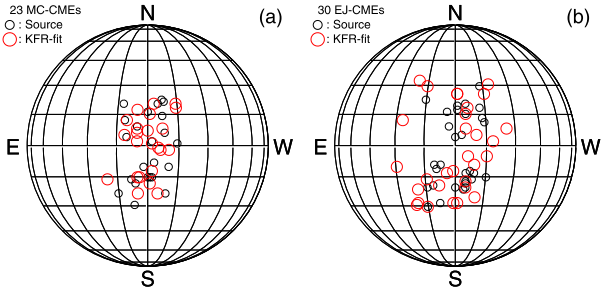

Figure 3 Comparison between the source locations (black circles) and the KFR-fit propagation directions (red circles) for (a) 23 MC-CMEs and (b) 30 EJ-CMEs.

relative to the E–W direction at 01:13 UT. The right panel shows the model outline curves (yellow curves) superimposed on a LASCO/C2 image at 00:54 UT. The fitting gave a CME radial speed $V_{\rm CME} = 1441$ km s^{-1}, $\omega_{\rm broad} = 90°$, and $\omega_{\rm edge} = 71°$; the best fit for the propagation direction was $(\lambda, \phi, \alpha) = (-25°, 10°, 60°)$. The fitting results showed that the CME erupted non-radially and was deflected from S13 to S25; the longitude and tilt angle of the KFR-fit direction were relatively consistent with the CME source location.

3. Statistical Analysis and Results

Table 1 summarizes the flux-rope fitting results for the 53 CMEs. Columns 1 – 8 are the event number, shock date, time, ICME type, CME date, first appearance time at LASCO C2, sky-plane speed, and source location identified based on solar surface activities: flare, EIT wave and dimming, eruptive prominence or disappearing filament. Columns 9 – 13 are outputs of the KFR-fit edge-on width and face-on (broadside) width, radial speed, propagation direction and tilt angle.

3.1. Spatial Relationship Between CME Source Locations and Propagation Directions

Previous studies have shown that CMEs may erupt non-radially and be deflected by the ambient magnetic environment such as coronal holes (*e.g.* Gopalswamy *et al.*, 2009; Mohamed *et al.*, 2012), streamers, and nearby ARs or complex intrinsic structures of associated ARs (*e.g.*, Xie *et al.*, 2009). Figure 3 shows the CME source locations (black circles) and the KFR-fit propagation directions (red circles) for (a) 23 MC-CMEs and (b) 30 EJ-CMEs. From Figure 3a we can see that both the CME source locations and the KFR-fit propagation directions for the MC-CMEs are relatively clustered close to disk center (DC).

Table 1 List of the CDAW 2011 CMEs and the best-fit flux-rope model parameters.

No.	ICME		Type[a]	CME				Flux-rope model fit output				
	Date	Time [UT]		Date	Time [UT]	V_{sky} [km s^{-1}]	Source	ω_e [◦]	ω_b [◦]	V_{cme} [km s^{-1}]	Direction	Tilt[b] [◦]
01	1997/01/10	00:52	MC	1997/01/06	15:10	136	S18E06	55	70	258	S18W01	−60.00
02	1997/05/15	01:15	MC	1997/05/12	05:30	464	N21W08	53	70	670	N01W02	−80.00
04	1998/05/03	17:00	EJ	1998/05/02	23:40	585	S18W05	79	90	826	S16E14	42.00
05	1998/05/04	02:00	EJ	1998/05/02	14:06	938	S15W15	79	90	2097	N08W05	22.00
07	1998/11/07	08:00	EJ	1998/11/04	07:54	523	N17W01	71	95	706	N25W01	92.00
08	1998/11/13	01:40	EJ	1998/11/09	18:18	325	N15W05	53	70	712	N15W05	16.00
09	1999/04/16	11:10	MC	1999/04/13	03:30	291	N16E00	79	90	560	S02W06	−10.00
10	1999/06/26	19:25	EJ	1999/06/24	13:31	975	N29W13	71	90	1531	N25W15	45.00
13	1999/09/22	12:00	EJ	1999/09/20	06:06	604	S20W05	31	70	868	S20W05	−35.00
14	1999/10/21	02:13	EJ	1999/10/18	00:06	144	S30E15	48	90	217	S30E15	60.00
15	2000/01/22	00:23	EJ	2000/01/18	17:54	739	S19E11	71	90	1179	S10E29	−25.00
16	2000/02/20	21:00	MC	2000/02/17	21:30	728	S29E07	71	84	994	S12W02	70.00
17	2000/07/10	06:00	EJ	2000/07/07	10:26	453	N04E00	48	90	739	S17W05	70.00
18	2000/07/11	11:22	EJ	2000/07/09	23:50	483	N18W12	58	77	1152	N18W06	15.00
19	2000/07/15	14:18	MC	2000/07/14	10:54	1674	N22W07	90	16	2281	N18W14	30.00
20	2000/07/26	18:58	EJ	2000/07/23	05:30	631	S13W05	71	84	1119	S13E04	−15.00
21	2000/07/28	06:39	MC	2000/07/25	03:30	528	N06W08	64	84	960	S15E04	−95.00
23	2000/08/11	18:51	MC	2000/08/09	16:30	702	N20E12	53	77	1024	N17E05	−85.00
24	2000/09/17	17:00	MC	2000/09/16	05:18	1215	N14W07	64	90	1574	N08W07	45.00
25	2000/10/05	03:23	EJ	2000/10/02	03:50	525	S09E07	53	90	1104	S19E08	−65.00
26	2000/10/12	22:36	MC	2000/10/10	23:50	798	N01W14	58	95	1287	N20W14	−55.00
27	2000/11/06	09:20	MC	2000/11/03	18:26	291	N02W02	64	87	542	N02E05	25.00

Table 1 (*Continued.*)

No.	ICME		Type[a]	CME				Flux-rope model fit output				
	Date	Time [UT]		Date	Time [UT]	V_{sky} [km s^{-1}]	Source	ω_e [◦]	ω_b [◦]	V_{cme} [km s^{-1}]	Direction	Tilt[b] [◦]
28	2000/11/26	05:30	EJ	2000/11/24	05:30	1289	N20W05	79	95	1745	N30W18	−55.00
29	2001/03/03	11:30	EJ	2001/02/28	14:50	313	S17W05	71	90	522	S05W15	−65.00
30	2001/03/22	14:00	EJ	2001/03/19	05:26	389	S20W00	71	90	691	N05W10	85.00
31	2001/04/11	14:12	EJ	2001/04/09	15:54	1192	S21W04	79	84	1813	S12E01	75.00
32	2001/04/11	16:19	MC	2001/04/10	05:30	2411	S23W09	71	95	3735	S23W05	−85.00
33	2001/04/28	05:02	MC	2001/04/26	12:30	1006	N20W05	79	77	1093	N20W03	30.00
34	2001/08/12	11:10	EJ	2001/08/09	10:30	479	N11W14	45	90	842	N02W18	80.00
35	2001/10/11	16:50	EJ	2001/10/09	11:30	973	S28E08	58	84	1449	S28E01	−20.00
36	2002/03/18	13:13	MC	2002/03/16	23:06	957	S08W03	79	00	1151	N15W01	−50.00
37	2002/04/17	11:01	MC	2002/04/15	03:50	720	S15W01	79	84	1302	S01W05	−10.00
38	2002/05/11	10:30	EJ	2002/05/08	13:50	614	S12W07	48	90	1231	S09W09	55.00
39	2002/05/18	19:51	MC	2002/05/16	00:50	600	S23E15	48	84	900	S23E05	−70.00
40	2002/05/20	03:40	EJ	2002/05/17	01:27	461	S20E14	31	66	743	S28E20	−60.00
41	2002/05/30	02:15	EJ	2002/05/27	13:27	1106	N22E15	58	84	1362	N32E20	80.00
42	2002/07/17	15:50	EJ	2002/07/15	21:30	1300	N19W01	90	95	2046	N29E15	−40.00
43	2002/08/01	05:10	MC	2002/07/29	12:07	222	S10W10	64	84	448	S02W10	−70.00
44	2003/08/17	13:40	MC	2003/08/14	20:06	378	S10E02	48	84	662	N12E10	−65.00
45	2003/10/29	06:00	MC	2003/10/28	11:30	2459	S16E08	90	90	2916	S16E20	75.00
46	2003/10/30	16:20	MC	2003/10/29	20:54	2029	S15W02	90	95	3474	S15E05	80.00
47	2004/01/22	01:10	EJ	2004/01/20	00:06	965	S13W09	90	71	1441	S25W10	60.00
48	2004/07/24	05:32	MC	2004/07/22	08:30	700	N04E10	71	84	1359	N06E05	−10.00
49	2004/11/09	09:05	MC	2004/11/06	02:06	1111	N09E05	90	95	1319	N07W00	12.00

Table 1 (*Continued.*)

No.	ICME		Type[a]	CME				Flux-rope model fit output				
	Date	Time [UT]		Date	Time [UT]	V_{sky} [km s^{-1}]	Source	ω_e [◦]	ω_b [◦]	V_{cme} [km s^{-1}]	Direction	Tilt[b] [◦]
50	2004/12/11	13:03	EJ	2004/12/08	20:26	611	N05W03	79	77	754	S05W06	45.00
51	2005/01/16	09:27	EJ	2005/01/15	06:30	2049	N16E04	58	84	2503	N25W01	−80.00
52	2005/02/17	21:59	EJ	2005/02/13	11:06	584	S11E09	60	84	587	S21E19	75.00
53	2005/05/15	02:19	MC	2005/05/13	17:12	1689	N12E11	90	90	2384	N05E11	45.00
54	2005/05/20	03:34	MC	2005/05/17	03:26	449	S15W00	64	84	596	N08E05	85.00
56	2005/07/10	02:56	EJ	2005/07/07	17:06	683	N09E03	48	87	1040	N12E26	91.00
57	2005/09/02	13:32	EJ	2005/08/31	11:30	825	N13W13	58	90	1161	N08W25	−5.00
58	2005/09/15	08:25	EJ	2005/09/13	20:00	1866	S09E10	79	95	2171	S29E21	−52.00
59	2006/08/19	10:51	EJ	2006/08/16	16:30	888	S16W08	71	90	1351	S28W01	−15.00

Notes:
Columns 1 – 4: the event number, shock date, time and ICME type. Columns 5 – 8: CME date, first appearance time at LASCO C2, sky-plane speed and source location. Columns 9 – 13: flux-rope model fit edge-on width, broadside width, radial speed, propagation direction and tilt angle.
[a]MC = Magnetic cloud; EJ = Ejecta.
[b]With respect to East clockwise.

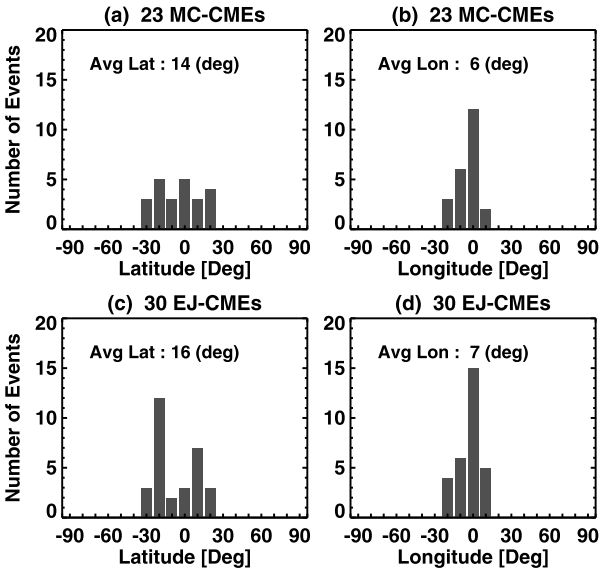

Figure 4 Histograms of the source locations: (a) latitude and (b) longitude for 23 MC-CMEs, (c) latitude and (d) longitude for 30 EJ-CMEs. The average absolute values are indicated in each plot.

Histograms of the source locations (Figures 4a and b) show that the mean absolute latitude and longitude of the source locations for the MC-CMEs are (14°, 6°); and the mean latitude and longitude of the KFR-fit propagation directions are (11°, 6°) (Figure 5a and b). While from Figure 3b, we see that the KFR-fit propagation directions of the EJ-CMEs are relatively scattered away from DC, compared to their source locations, indicating some degree of CME deflection. These deflections of the EJ-CMEs are also shown in Figure 5. In Figure 4 the mean latitude and longitude of the source locations for the EJ-CMEs are (16°, 7°), but the mean latitude and longitude of the KFR-fit propagation directions for the EJ-CMEs are (18°, 11°) (Figure 5c and d).

Figure 6 plots histograms of: (a) $\Delta_{\rm lat}$ and (b) $\Delta_{\rm lon}$ for 23 MC-CMEs, and (c) $\Delta_{\rm lat}$ and (d) $\Delta_{\rm lon}$ for 30 EJ-CMEs, where $\Delta_{\rm lat} = |Lat_{\rm fr}| - |Lat_{\rm sc}|$ and $\Delta_{\rm lon} = |Lon_{\rm fr}| - |Lon_{\rm sc}|$ are the latitudinal and longitudinal differences between CME source locations ($Lat_{\rm sc}$, $Lon_{\rm sc}$) and KFR-fit propagation directions ($Lat_{\rm fr}$, $Lon_{\rm fr}$). The mean $\Delta_{\rm lat}$ and $\Delta_{\rm lon}$ for the MC-CMEs are $-2.7°$ and $-0.3°$, and the mean $\Delta_{\rm lat}$ and $\Delta_{\rm lon}$ for the EJ-CMEs are 2.0° and 4.1°. Since positive (negative) values of $\Delta_{\rm lat}$ and $\Delta_{\rm lon}$ indicate that the CMEs were deflected away from (towards) DC, both Figure 5 and Figure 6 suggest that the EJ-CMEs were deflected farther from DC while the MC-CMEs were deflected closer to DC during their eruption and propagation near the Sun.

3.2. Comparison of Angular Widths Between MC-CMEs and EJ-CMEs

Figure 7 presents histograms of (a) $\omega_{\rm edge}$ and (b) $\omega_{\rm broad}$ for 23 MC-CMEs, and histograms of (c) $\omega_{\rm edge}$ and (d) $\omega_{\rm broad}$ for 30 EJ-CMEs, where $\omega_{\rm edge}$ and $\omega_{\rm broad}$ are the KFR-fit widths of the CMEs from edge-on and face-on views, respectively. The mean broadside (face-on) widths are 87° and 85° for the MC-CMEs and EJ-CMEs, and the mean edge-on widths are 70° and 63° for the MC-CMEs and EJ-CMEs, respectively. The MC-CMEs are wider than the EJ-CMEs by 2° in the mean broadside width and 7° in the mean edge-on width. This indicates that the MC-CMEs are not only deflected toward DC, but also are slightly larger in widths, thus their central FR structures are more likely observed *in-situ*.

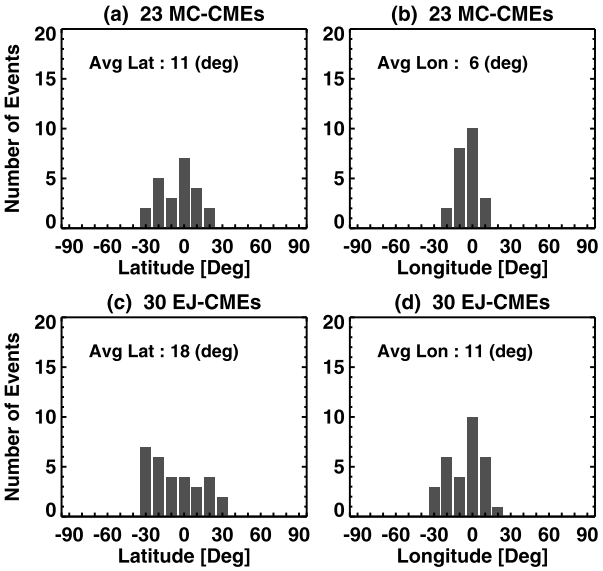

Figure 5 Histograms of the KFR-fit propagation directions: (a) latitude and (b) longitude for 23 MC-CMEs, (c) latitude and (d) longitude for 30 EJ-CMEs. The average absolute values are indicated in each plot.

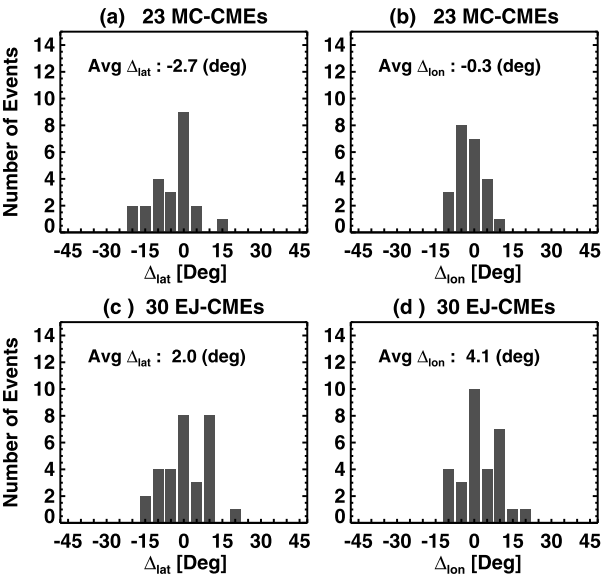

Figure 6 Histograms of latitudinal difference between the CME source locations and propagation directions Δ_{lat} for (a) 23 MC-CMEs and (c) 30 EJ-CMEs, and histograms of longitudinal difference Δ_{lon} for (b) 23 MC-CMEs and (d) 30 EJ-CMEs. The average values are indicated in each plot.

3.3. Comparison of Radial Speeds Between MC-CMEs and EJ-CMEs

Figure 8 shows histograms of radial speeds for: (a) 23 MC-CMEs and (b) 30 EJ-CMEs. The mean radial speeds are 1369 km s^{-1} and 1190 km s^{-1} for the MC-CMEs and EJ-CMEs, respectively. The MC-CMEs are faster than EJ-CMEs by 121 km s^{-1} concerning their mean radial speeds. This might be one of other factors affecting the observed ICME properties. It is expected that the FR structures in the slow CMEs become more distorted by their interactions with the background solar wind and/or with other CMEs (*cf.*, Kim *et al.*, 2012) during their propagation.

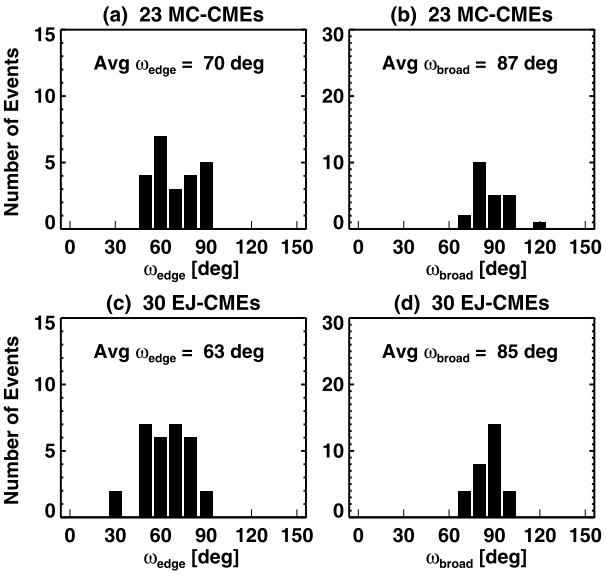

Figure 7 Histograms of KFR-fit widths: (a) edge-on width ω_{edge} and (b) broadside width ω_{broad} for 23 MC-CMEs, (c) ω_{edge} and (d) ω_{broad} for 30 EJ-CMEs. The average values are indicated in each plot.

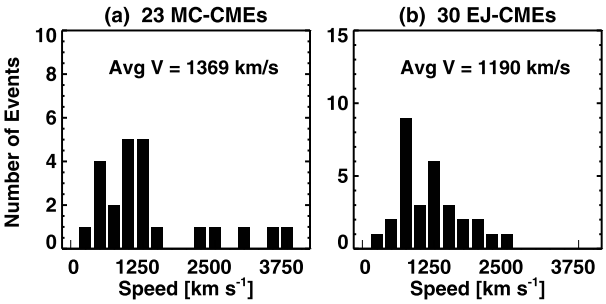

Figure 8 Histograms of KFR-fit radial speed V_{cme} for (a) 23 MC-CMEs and (b) 30 EJ-CMEs. The average values are indicated in each plot.

4. Summary and Conclusion

We studied a set of the CDAW 2011 CMEs which consisted of 23 MC-CMEs and 30 EJ-CMEs. These two groups of CMEs originated from similar source locations, with mean latitude and longitude of the MC-CMEs (EJ-CMEs) of 14 (16)° and 6 (7)°, respectively. We applied the KFR-fit to determine the CME radial speeds, angular widths, and propagation directions. The KFR-fit results have revealed that the properties of these two groups of CMEs showed no characteristic differences.

However, there exist distinguishing features between the two groups in terms of their propagation directions and angular widths. It is found that the EJ-CMEs tend to propagate in higher latitudinal and longitudinal directions. The mean propagation latitude and longitude of the EJ-CMEs were larger than those of the MC-CMEs by 7° and 5° (Figure 5), respectively. The likely reasons of the CME non-radial eruption are the complex intrinsic structures of the associated ARs, deflections from the ambient magnetic structures such as coronal holes, streamers, and nearby ARs. It is shown in Figure 6 that the EJ-CMEs were deflected away from DC, while the MC-CMEs were deflected towards DC. Similar results are also found in Gopalswamy *et al.* (2009) and Mohamed *et al.* (2012), where they studied the interaction of CMEs with coronal holes. Gopalswamy *et al.* (2009) showed that some fast

and wide CMEs from DC were deflected away from the Sun–Earth line and the spacecraft at L1 only observed driveless-like shocks. Mohamed *et al.* (2012) calculated the coronal hole deflection parameters, which are smaller for MCs. The non-radial eruption and deflection of the CMEs has caused the FR eruptions originating from near DC to propagate away from DC and the observing spacecraft passed only by their flank and missed the central FR structures. In addition, the MC-CMEs were also found to be wider than the EJ-CMEs. The mean broadside and edge-on widths of the MC-CMEs were larger than those of the EJ-CMEs by 2° and 7°, respectively. The obtained results suggest that the FR structures in the MC-CMEs are caught *in-situ* not only because they were deflected toward DC, but also because they were larger in size.

In conclusion, both the MC-CMEs and EJ-CMEs had similar solar sources and possible flux-rope structures; their different propagation directions and angular widths determine whether they are viewed as clouds or non-clouds by the observing spacecraft. The results of this work support the conjecture that "all CMEs have flux-rope structure".

Acknowledgements This work uses data from the NASA/LWS Coordinated Data Analysis Workshops on CME/flux-ropes in 2010 and 2011. We acknowledge the workshop support provided by NASA/LWS, Predictive Sciences, Inc. (San Diego, CA), University of Alcala (Alcala de Henares, Spain), and Ministerio de Ciencia e Innovacion (Reference number AYA2010-12439-E), Spain. The authors acknowledge support of NASA grant LWSTRT08-0029.

References

Burkepile, J.T., Hundhausen, A.J., Stanger, A.L., St. Cyr, O.C., Seiden, J.A.: 2004, Role of projection effects on solar coronal mass ejection properties: 1. A study of CMEs associated with limb activity. *J. Geophys. Res.* **109**, 3103. doi:10.1029/2003JA010149.

Burkepile, J.T., St. Cyr, O.C.: 1993, A revised and expanded catalogue of mass ejections observed by the Solar Maximum Mission coronagraph. NASA STI/Recon Technical Report N 93, 26556.

Burlaga, L., Sittler, E., Mariani, F., Schwenn, R.: 1981, Magnetic loop behind an interplanetary shock – Voyager, Helios, and IMP 8 observations. *J. Geophys. Res.* **86**, 6673 – 6684. doi:10.1029/JA086iA08p06673.

Chen, J., Howard, R.A., Brueckner, G.E., Santoro, R., Krall, J., Paswaters, S.E., St. Cyr, O.C., Schwenn, R., Lamy, P., Simnett, G.M.: 1997, Evidence of an erupting magnetic flux rope: LASCO coronal mass ejection of 1997 April 13. *Astrophys. J. Lett.* **490**, L191. doi:10.1086/311029.

Cremades, H., Bothmer, V.: 2004, On the three-dimensional configuration of coronal mass ejections. *Astron. Astrophys.* **422**, 307 – 322. doi:10.1051/0004-6361:20035776.

Dere, K.P., Brueckner, G.E., Howard, R.A., Michels, D.J., Delaboudiniere, J.P.: 1999, LASCO and EIT observations of helical structure in coronal mass ejections. *Astrophys. J.* **516**, 465 – 474. doi:10.1086/307101.

Gibson, S.E., Low, B.C.: 2000, Three-dimensional and twisted: an MHD interpretation of on-disk observational characteristics of coronal mass ejections. *J. Geophys. Res.* **105**, 18187 – 18202. doi:10.1029/1999JA000317.

Gopalswamy, N.: 2006, Properties of interplanetary coronal mass ejections. *Space Sci. Rev.* **124**, 145 – 168. doi:10.1007/s11214-006-9102-1.

Gopalswamy, N., Mäkelä, P., Xie, H., Akiyama, S., Yashiro, S.: 2009, CME interactions with coronal holes and their interplanetary consequences. *J. Geophys. Res.* **114**, A00A22. doi:10.1029/2008JA013686.

Gopalswamy, N., Xie, H., Mäkelä, P., Akiyama, S., Yashiro, S., Kaiser, M.L., Howard, R.A., Bougeret, J.-L.: 2010, Interplanetary shocks lacking type II radio bursts. *Astrophys. J.* **710**, 1111 – 1126. doi:10.1088/0004-637X/710/2/1111.

Gosling, J.T.: 1990, *Coronal Mass Ejections and Magnetic Flux Ropes in Interplanetary Space*. *Geophys. Monogr. Ser.* **58**, AGU, Washington, 343 – 364.

Illing, R.M.E., Hundhausen, A.J.: 1985, Observation of a coronal transient from 1.2 to 6 solar radii. *J. Geophys. Res.* **90**, 275 – 282. doi:10.1029/JA090iA01p00275.

Kim, R.-S., Gopalswamy, N., Cho, K.-S., Moon, Y.-J., Yashiro, S.: 2012, Different characteristics of MC associated CME and EJ associated CME. *Solar Phys.*, submitted (this issue).

Krall, J.: 2007, Are all coronal mass ejections hollow flux ropes? *Astrophys. J.* **657**, 559 – 566. doi:10.1086/510191.

Krall, J., St. Cyr, O.C.: 2006, Flux-rope coronal mass ejection geometry and its relation to observed morphology. *Astrophys. J.* **652**, 1740 – 1746. doi:10.1086/508337.

Krall, J., Chen, J., Duffin, R.T., Howard, R.A., Thompson, B.J.: 2001, Erupting solar magnetic flux ropes: theory and observation. *Astrophys. J.* **562**, 1045 – 1057. doi:10.1086/323844.

Mohamed, A.A., Gopalswamy, N., Yashiro, S., Akiyama, S., Mäkelä, P., Xie, H., Jung, H.: 2012, The relation between coronal holes and coronal mass ejections during the rise, maximum, and declining phases of Solar Cycle 23. *J. Geophys. Res.* **117**, 1103. doi:10.1029/2011JA016589.

St. Cyr, O.C., Plunkett, S.P., Michels, D.J., Paswaters, S.E., Koomen, M.J., Simnett, G.M., Thompson, B.J., Gurman, J.B., Schwenn, R., Webb, D.F., Hildner, E., Lamy, P.L.: 2000, Properties of coronal mass ejections: SOHO LASCO observations from January 1996 to June 1998. *J. Geophys. Res.* **105**, 18169 – 18186. doi:10.1029/1999JA000381.

St. Cyr, O.C., Cremades, H., Bothmer, V., Krall, J., Burkepile, J.T.: 2004, Morphology Indicators of the three-dimensional size of flux rope CMEs: a prediction for STEREO. AGU Fall Meeting Abstracts, SH22A-04.

Thernisien, A.F.R., Howard, R.A., Vourlidas, A.: 2006, Modeling of flux rope coronal mass ejections. *Astrophys. J.* **652**, 763 – 773. doi:10.1086/508254.

Xie, H., St. Cyr, O.C., Gopalswamy, N., Yashiro, S., Krall, J., Kramar, M., Davila, J.: 2009, On the origin, 3D structure and dynamic evolution of CMEs near solar minimum. *Solar Phys.* **259**, 143 – 161. doi:10.1007/s11207-009-9422-x.